Scaling and design of miniature high-speed bearingless slice motors

M. Schuck IEEE, P. Puentener IEEE, T. Holenstein IEEE, J. W. Kolar IEEE

Recent years have shown a development of electrical drive systems toward high rotational speeds to increase the power density. Applications such as optical systems benefit from rotational speeds at which conventional ball bearings suffer from high losses, excessive wear, and decreased reliability. In such cases, magnetic bearings offer an interesting alternative. This work presents a universally applicable design procedure for miniature bearingless slice motors intended for rotational speeds of several hundred thousand revolutions per minute. Design trade-offs are illustrated and facilitate the selection of Pareto-optimal implementations. An exemplary motor prototype for rotational speeds of up to 760 000 rpm with a rotor diameter of 4 mm and a suitable inverter featuring an FPGA-based controller are demonstrated briefly.

Keywords: bearingless machine; high rotational speed; optimization; scaling laws; slice motor; slotless

Skalierung und Auslegung von lagerlosen Miniatur-Scheibenläufermotoren für hohe Drehzahlen.

Um die Leistungsdichte elektrischer Antriebssysteme zu erhöhen, existiert seit einigen Jahren ein Trend hin zu höheren Rotationsgeschwindigkeiten solcher Motoren. Anwendungen wie beispielsweise optische Systeme profitieren von hohen Rotationsgeschwindigkeiten, bei denen konventionelle Kugellager mit hohen Verlusten, überhöhtem Verschleiß und verringerter Zuverlässigkeit behaftet sind. In solchen Fällen bieten Magnetlager eine interessante Alternative. Die vorliegende Arbeit präsentiert einen universell einsetzbaren Designprozess für lagerlose Scheibenläufermotoren kleiner Baugröße, die für den Einsatz bei Drehzahlen von mehreren Hunderttausend Umdrehungen pro Minute vorgesehen sind. Eine Veranschaulichung der bei der Auslegung solcher Maschinen einzugehenden Kompromisse ermöglicht die Realisierung von Pareto-optimalen Designs. Ein beispielhafter Prototyp eines Motors für Drehzahlen von bis zu 760 000 U/min und einem Rotordurchmesser von 4 mm sowie ein geeigneter Umrichter mit FPGA-basierter Regelung werden kurz beschrieben.

Schlüsselwörter: hohe Drehzahlen; lagerloser Motor; nutenlos; Optimierung; Scheibenläufermotor; Skalierungsgesetze

Check for updates

1. Introduction

Several applications, such as turbocompressors [15], machining spindles [14], flywheels and reaction wheels [9, 37], as well as generators for micro gas turbines [8], have fueled a trend toward the miniaturization of electric drive systems. To deliver the desired power level at a small size, a high power density of the employed electric machine is required, which can be achieved by operation at high rotational speeds [28, 38]. Independent from the requirement of obtaining high power densities, applications such as optical systems that feature rotating polygon mirrors [7] and lightweight reaction wheels for attitude control of small spacecrafts [13] directly require high rotational speeds of up to several hundred thousand revolutions per minute (rpm) for small-scale machines.

At these rotational speeds, the use of conventional ball bearings entails significant disadvantages, such as excessive wear, decreased reliability, and a shortened lifetime. The application of gas bearings, in which the spinning rotor is supported by a fluid film [16], to miniature motors is limited by unfeasible production tolerances.

Active magnetic bearings (AMBs) support the rotor without mechanical contact by means of magnetic forces and do not exhibit these disadvantages [32]. However, their use results in an increased size and overall complexity of the electric drive system, as generally all degrees of freedom of the rotor have to be actively stabilized [1]. For a conventional machine design with a shaft rotor, the achievable rotational speed is commonly limited by the critical frequency at

which bending of the rotor occurs [4]. AMBs further limit the miniaturization potential of such machines due to the required complex rotor construction.

Slice motors feature a rotor length that is smaller than the rotor radius and do not exhibit these drawbacks. Due to the geometry of the motor, the rotor is passively stable in the axial and tilting directions and only the radial degrees of freedom have to be stabilized by an AMB [29]. The rotor can consist of a single diametrically-magnetized permanent magnet (PM) and the achievable rotational speed is ultimately limited only by the mechanical stress due to the centrifugal force that the rotor material can withstand. Highly compact designs are possible by employing the same magnetic circuit and the same stator windings for generating the motor torque and magnetic bearing force [20, 27]. Such a topology is referred to as *bearingless*. Initial designs of slice motors employed slotted stators to accommodate the machine windings. The slots result in eddy current losses due to stator harmonics, particularly at high field frequencies as required for achieving high rotational speeds. Therefore, a slotless stator de-

Schuck, Marcel, Power Electronic Systems Laboratory, ETH Zurich, Technoparkstrasse 1, 8005 Zurich, Switzerland (E-mail: schuck@lem.ee.ethz.ch); **Puentener, Pascal,** Power Electronic Systems Laboratory, ETH Zurich, Technoparkstrasse 1, 8005 Zurich, Switzerland; **Holenstein, Thomas,** Power Electronic Systems Laboratory, ETH Zurich, Technoparkstrasse 1, 8005 Zurich, Switzerland; **Kolar, Johann W.,** Power Electronic Systems Laboratory, ETH Zurich, Technoparkstrasse 1, 8005 Zurich, Switzerland
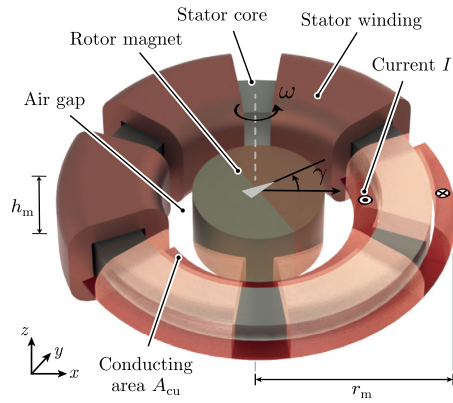
Fig. 1. Schematic view of the slotless bearingless slice motor topology

sign with toroidally-wound coils as shown in Fig. 1 is considered in this work.

Several motor prototypes that use this topology and reach rotational speeds above 100 000 rpm have been presented in the literature. In [21] a rotational speed of 115 000 rpm was reached with a rotor diameter of 32 mm in a compressor application. A rotational speed of up to 140 000 rpm is reported in [33] in a textile spinning application. Recently, a demonstrator system reaching 150 000 rpm with a rotor diameter of 22 mm has been presented [26]. Further miniaturization of this design to a rotor diameter of 4 mm has been reported in [30], where it was shown that uniform scaling of all machine dimensions is not possible for such miniature motors due to mechanical tolerances. This was also encountered in [34], which considers the miniaturization of the motor presented in [35].

This paper outlines the scaling laws of electrical machines with a focus on miniature bearingless slice motors. The key design challenges are identified and a novel unified optimization procedure based on analytical models for the motor properties and losses as well as 3D finite element method (FEM) simulations is presented. An exemplary motor design with an outer diameter of less than 30 mm and the corresponding inverter are briefly presented. Potential application areas of the demonstrated machine are small size flywheels and reaction wheels, optical systems, as well as hyper-gravity science.

2. Scaling laws
This section outlines the scaling laws that govern the torque and power generation of an electric motor and their particular implications for millimeter-scale bearingless slice motors are discussed.

2.1 General scaling laws of electric machines
For the purpose of deriving the general scaling laws, the electric machine with PM rotor shown in Fig. 1 is considered. Non-idealities, such as stray fields, are neglected at this point. The motor has an outer surface area $A_m = 2\pi r_m^2 + \pi r_m h_m$ and volume $V_m = \pi r_m^2 h_m$, where r_m and h_m denote the outer radius and axial length, respectively. If the machine is scaled uniformly with the ratio of all dimensions remaining constant, it is sufficient to consider a single dimensional scaling factor x_d, yielding $A_m \propto x_d^2$ and $V_m \propto x_d^3$. The achievable angular rotational frequency of the rotor $\omega = 2\pi f = v_c/r_r$, where r_r denotes the rotor radius, is ultimately limited by the circumferential speed v_c that the rotor material can withstand before mechanical failure due to centrifugal forces occurs, resulting in $n_{max} \propto x_d^{-1}$ for the maximum rotational speed.

The current I that flows in the stator windings of the machine to generate a torque can equivalently be considered to be distributed across the cross-sectional copper area A_{cu} inside the stator bore, as schematically depicted in Fig. 1. Consequently, the resulting conduction losses can be obtained as

$$P_{cu} = RI^2 \quad \text{with } R = \rho_{cu}\frac{h_{cu}}{A_{cu}} \propto x_d^{-1}, \tag{1}$$

where ρ_{cu} denotes the resistivity of copper and h_{cu} is the axial length of the conducting surface.

Additional losses occur in the stator core, which can be modeled using the empirical Steinmetz equation

$$P_c = C_m V_c f^\alpha \hat{B}^\beta, \tag{2}$$

where C_m, α, β, and V_c denote the Steinmetz coefficients and the volume of the stator core, respectively. For the fundamental frequency of the magnetic field $f \propto x_d^{-1}$ holds, as outlined above. For the miniature high-speed motors considered in this work, Metglas 2605SA1 amorphous alloy [19] constitutes a suitable material for the stator core as it features significantly lower core losses compared to conventional sheeted electrical steel at high field frequencies. The Steinmetz coefficients for this material are listed in Table 1. The overall core losses are comprised of hysteresis losses P_{hy}, eddy current losses P_{ed}, and excess losses P_e, where the latter stem from microscopic phenomena in the ferromagnetic material. Employing a loss model that considers these components separately [2] results in

$$P_c = \underbrace{k_{hy}V_c f\hat{B}^{\beta'}}_{P_{hy}} + \underbrace{k_{ed}V_c f^2\hat{B}^2}_{P_{ed}} + \underbrace{k_e V_c f^{1.5}\hat{B}^{1.5}}_{P_e}. \tag{3}$$

Commonly, $\beta' = 2$ is assumed, which corresponds to an approximation of the actual hysteresis loop by an ellipse. The values of the constants k_{hy}, k_{ed}, and k_e for this case have been added to Table 1. Consequently, the scaling laws for the individual loss components can be derived as

$$P_{hy} \propto x_d^2, \quad P_{ed} \propto x_d, \quad \text{and} \quad P_e \propto x_d^{1.5}. \tag{4}$$

It can be seen that the eddy current losses constitute a higher portion of the overall core losses for smaller machines, while the hysteresis losses become less relevant. The differences between the absolute values of the loss components, however, are less pronounced, as k_{ed} and k_e are four and two orders of magnitude smaller than k_{hy}, respectively.

In addition to the aforementioned losses, windage losses P_w due to air friction occur at the cylindrical surface of the rotor and at its faces (base of the cylinder) and can be expressed as

$$P_{w,c} = k_r C_f \rho_{air} \pi \omega^3 r_r^4 h_r \tag{5}$$

and

$$P_{w,b} = \frac{1}{2}k_r C_f \rho_{air}\omega^3 r_r^5, \tag{6}$$

respectively. Here, k_r, C_f, ρ_{air}, and h_r denote the roughness coefficient of the rotor surface, an empirically obtained friction coefficient, the density of air, and the axial length of the rotor, respectively. It can be seen that $P_w \propto x_d^2$ holds. However, models for obtaining C_f for
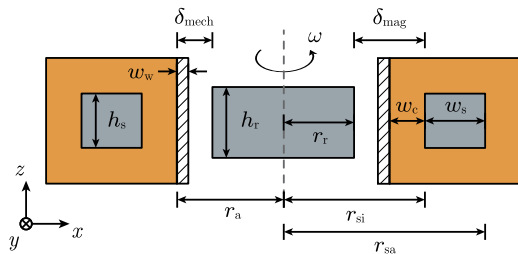
Fig. 2. Geometrical design parameters of the motor

Table 2. Scaling of design parameters for slotless bearingless slice motors

	d_r	δ_{mech}	h_r/r_r	h_s/h_r	δ_{mag}/r_r	n_{max}
[35]	102 mm	2 mm	0.29	0.83	0.19	20 000 rpm
[26]	22 mm	1.4 mm	0.82	0.89	0.41	150 000 rpm
[30]	4 mm	1 mm	1	0.75	0.88	760 000 rpm

various flow conditions of the surrounding air usually contain further geometrical parameters of the motor [3, 5].

The admissible overall losses of the motor are limited by the heat transfer rate $\dot{Q}_c$ between the machine and its environment. Heat transfer occurs across the surface area, resulting in $\dot{Q}_c \propto x_d^2$. The stator core needs to be designed such that the core losses P_c are sufficiently low and a suitable material that features low eddy current losses (low sheet thickness/power ferrite) has to be used for high speed machines. The most critical scaling behavior is exhibited by the resistance of the machine windings ($R \propto x_d^{-1}$). To fulfill the condition $P_{cu} \leq \dot{Q}_c$, the admissible current is limited to $I \propto x_d^{1.5}$. By considering the Lorentz force resulting from the interaction of the radial component $B_{a,r}$ of the PM flux density in the airgap with the current I, the motor torque can be obtained as

$$T = B_{a,r} I h_s \bar{r} \propto x_d^{3.5}, \tag{7}$$

where $I \propto x_d^{1.5}$ has been used and h_s, $\bar{r}$ denote the height of the stator core and average radius of the stator windings inside the bore, respectively. The output power of the machine is given as $P = T\omega$. Using the aforementioned scaling law for ω results in $P \propto x_d^{2.5}$. Consequently, the power density is obtained as

$$p = \frac{P}{V_m} \propto x_d^{-0.5} \tag{8}$$

if the considered machine is operated at the maximum admissible circumferential speed of the rotor. This shows that small-scale machines operating at high rotational speeds are favorable for achieving high power densities.

2.2 Application to bearingless slice motors

Due to lower bounds on the achievable mechanical tolerances, it is not easily possible to scale all dimensions of the machine by the same factor for miniature motors. Figure 2 shows a cross-sectional view of the bearingless slice motor topology including its geometrical parameters. The parameters w_c and w_s denote the width of the coil and the stator core in the radial direction, respectively. The radii r_a, r_{si}, and r_{sa} denote the inner radius of the coils, the inner radius of the stator core, and the outer radius of the stator core, respectively. The mechanical air gap δ_{mech} of bearingless machines cannot be reduced arbitrarily, as it has to accommodate a stator wall with a certain minimum thickness w_w. This wall is required as the motor is not equipped with backup or touchdown bearings. This means that the rotor is attracted to this wall once the active magnetic bearing that stabilizes the radial degrees of freedom is turned off. Without a stator wall, the rotor would get in direct contact with the stator windings, resulting in potential damage. Moreover, in a slotless motor topology, sufficient space for the windings needs to be provided between the rotor and the stator core, resulting in a large magnetic air gap δ_{mag}.

To analyze this dependency, Table 2 lists the relevant dimensional ratios of three slotless bearingless slice motors published in the literature. It can be observed that the mechanical air gap δ_{mech} remains relatively constant, despite a significant reduction of the rotor diameter. Moreover, the height-to-radius ratio of the rotor increases, which requires careful consideration of the passive stability properties as outlined in Section 3. The most pronounced increase can be observed for the ratio between the length of the magnetic air gap and the rotor radius (δ_{mag}/r_r), which reaches values that are unusually high for electric machines at small rotor diameters. Consequently, scaling is not straightforward as the value of δ_{mag} significantly influences the passive and active motor properties. Instead, a comprehensive design procedure that considers the dependency of the magnetic field on the air gap length is required.

3. Design equations

The operating principle of slotless bearingless slice motors has been described in [21, 35], which can be referred to for details. In this section, the design equations that are used in the optimization procedure described in Section 5 are outlined. Analytical models are used where possible, as they allow for the rapid assessment of a large number of design variations. In the cases where an analytical solution to the underlying problem cannot easily be obtained, e.g. for the passive properties of the motor, 3D FEM simulations are used.

3.1 Mechanical stress and rotor diameter

During rotation the maximum mechanical stress σ_{max} occurs along the axis of rotation and can be calculated as

$$\sigma_{max} = C_s \rho_r \omega^2 r_r^2, \tag{9}$$

where C_s and ρ_r denote a shape constant and the density of the rotor material, respectively. Various constructive means to increase the mechanical strength of the rotor, such as applying a titanium sleeve [38] or carbon fiber bandage [21], have been presented in the literature. However, their application becomes increasingly difficult at decreasing rotor size due to low mechanical tolerances and is, therefore, not considered in this work. For a disk-shaped rotor with $h_r \ll r_r$

$$C_s = \frac{3 + \nu}{8} \tag{10}$$

holds, where ν denotes the Poisson's ratio [11]. The aforementioned geometrical constraint $h_r \ll r_r$ is not fulfilled for small-size slice motors. However, an assessment by means of mechanical 3D FEM simulations shows that for NdFeB PM material ($\nu = 0.24$) the solution obtained by (10) is less than 5% lower than the actual value for $h_r = r_r$, thus providing a sufficiently accurate estimate.

Using $\sigma_s \approx 80$ MPa for the tensile strength of the rotor material and $\rho_r = 7\,500$ kg/m³ [12] yields a maximum achievable circumferential speed of $v_c \approx 160$ m/s. Consequently,

$$r_r < \frac{1}{\omega} \sqrt{\frac{8\sigma_s}{(3 + \nu)\rho_r}} \tag{11}$$
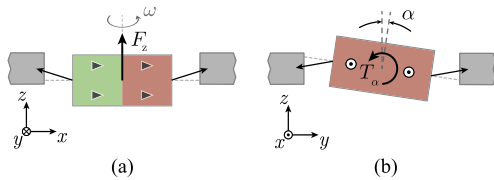
Fig. 3. Passive axial stiffness (a) and tilting stiffness around the axis of magnetization (b)

has to hold for a desired rotational speed in order to prevent mechanical failure.

3.2 Passive stability properties

The passively generated stabilizing restoring forces due to an axial deflection (see Fig. 3(a)) or tilting (see Fig. 3(b)) of the rotor are quantified by passive stiffnesses defined as

$$k_z = -\frac{dF_z}{dz} \tag{12}$$

in the axial direction and

$$k_\alpha = -\frac{dT_\alpha}{d\alpha} \text{ and } k_\beta = -\frac{dT_\beta}{d\beta} \tag{13}$$

in the tilting directions, where α and β denote the tilting angles around the magnetization direction (d-axis) and perpendicular to the magnetization direction (q-axis) of the rotor, respectively. For a rotor with a single pole pair $k_\alpha < k_\beta$ holds, as the change of the axial component of the magnetic field is smaller if the rotor is tilted around its d-axis. Consequently, k_α has to be considered during the design procedure of the machine. The passive stiffness k_z has to be sufficiently high to support the weight of the rotor (for a vertically aligned motor) and the application-dependent axial load. Providing a lower bound for the tilting stiffness is not straightforward as it strongly depends on the application conditions. A pure tilting movement of the rotor during operation is usually prevented by the gyroscopic effect, especially at high rotational speeds. Instead, weakly damped precession movements may be observed [22].

In addition to the aforementioned stabilizing forces, destabilizing passive radial forces act on the rotor if it is displaced from its equilibrium position in the radial center of the stator. The corresponding stiffnesses along the d- and q-axis are defined as

$$k_d = -\frac{dF_d}{dd} \quad \text{and} \quad k_q = -\frac{dF_q}{dq}, \tag{14}$$

respectively, where $k_q < k_d$ holds. If the active radial magnetic bearing is turned off, the rotor is pulled against the stator wall with a force F_w that depends on the design of the motor. The value of k_d has to be sufficiently low, such that the rotor can safely be detached from the stator wall by the magnetic bearing force F_{amb} during the start-up process of the motor, i.e. $F_{amb} > F_w$ has to hold.

The attainable bearing force depends on motor design parameters, such as the number of turns of the stator windings, but is essentially limited by the current driving capability of the employed inverter. As the start-up process is short, high coil currents can usually be tolerated from a thermal standpoint. Therefore, a conclusive assessment also requires knowledge of the inverter properties.

3.3 Magnetic field

The magnetic field inside the motor has to be obtained separately for the regions of the magnetic air gap and the stator core. The flux density in the air gap is used to calculate the motor torque, while the field distribution in the stator core is used to obtain the stator

losses. In accordance with [17], it was found that the magnetic field inside the motor with an air-gap winding is mainly caused by the rotor PM, while the influence of the stator field can be neglected for the calculations. An overview of existing analytical models that consider the field distribution in a radial plane inside a slotless machine is provided in [25]. For the subsequent calculations, a relative permeability of $\mu_r = 1$ in the magnetic airgap, the simplifying assumption of $\mu_r \to \infty$ for the stator material, and a rotor angle of $\gamma = 0$ are considered.

The components of the magnetic flux density in the magnetic airgap region ($r_r < r < r_{si}$) are calculated as

$$B_{a,r}(r,\varphi) = \frac{B_{rem}}{2}\left(\frac{r_r}{r_{si}}\right)^2 \cdot \left[1+\left(\frac{r_{si}}{r}\right)^2\right]\cos(\varphi), \tag{15}$$

$$B_{a,\varphi}(r,\varphi) = \frac{B_{rem}}{2}\left(\frac{r_r}{r_{si}}\right)^2 \cdot \left[1-\left(\frac{r_{si}}{r}\right)^2\right]\sin(\varphi), \tag{16}$$

where r, φ, and B_{rem} denote the variables of a cylindrical coordinate system and the remnant magnetic flux density of the rotor magnet, respectively. The components of the magnetic flux density as caused by the PM in the stator core ($r_{si} \leq r \leq r_{sa}$) are obtained as

$$B_{s,r}(r,\varphi) = \left(\frac{B_{rem}r_r^2}{r_{sa}^2-r_{si}^2}\right) \cdot \left[1-\left(\frac{r_{sa}}{r}\right)^2\right]\cos(\varphi), \tag{17}$$

$$B_{s,\varphi}(r,\varphi) = \left(\frac{B_{rem}r_r^2}{r_{sa}^2-r_{si}^2}\right) \cdot \left[1+\left(\frac{r_{sa}}{r}\right)^2\right]\sin(\varphi). \tag{18}$$

3.4 Motor torque

Based on the interaction of the radial component of the magnetic flux density in the air gap (15) with the stator current, the electromagnetic torque is obtained as

$$T = h_s \int_0^{2\pi}\int_{r_a}^{r_{si}} k_f k_w B_{a,r}(r,\varphi)J(\varphi)r^2 \, dr \, d\varphi, \tag{19}$$

where k_f and k_w denote the fill factor of the windings and the winding factor, respectively. The current density caused by the drive current can be written as $J(\varphi) = \hat{J}\cos(\varphi)$. Solving (19) yields:

$$T = h_s\frac{B_{rem}}{2}\left(\frac{r_r}{r_{si}}\right)^2 k_f k_w \hat{J}\pi\left[\frac{r_{si}^3-r_a^3}{3}+r_{si}^2(r_{si}-r_a)\right]. \tag{20}$$

4. Loss models

Models of the occurring losses in the motor are necessary to calculate the efficiency of a design. The most relevant loss components for the considered motor topology are copper losses P_{cu} in the windings and losses in the stator core P_c due to eddy currents and hysteresis.

4.1 Copper losses

The copper losses are constituted of conduction losses due to the ohmic dc resistance of the winding

$$P_{cu} = 6\rho_{cu}(\theta)lA_{cu}J_{rms}^2, \tag{21}$$

where $\rho_{cu}(\theta)$, l, and A_{cu} denote the temperature-dependent resistivity of copper, the wire length per coil, and the copper area per coil, respectively. The winding temperature is estimated by a thermal model (see below). Additional losses occur in the windings due to the skin and proximity effects, which are caused by eddy currents mainly due to the PM field of the rotor penetrating the windings. These losses can be assessed by using the methodologies presented in [10, 24] and obtaining the values of the magnetic flux density in the windings based on (15) and (16). The overall copper losses are minimized during the machine design by choosing a litz wire with a suitable strand diameter and number of strands for the stator coils.
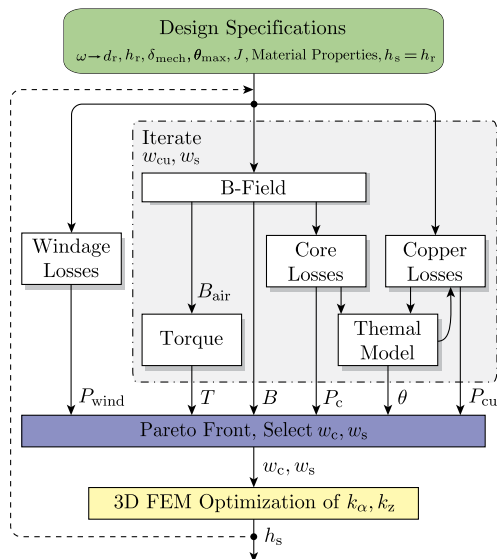
Fig. 4. Flow diagram of the design procedure

A trade-off between low eddy current losses and a decreased fill factor k_f causing higher conduction losses for smaller strand diameters exists.

4.2 Core losses

Losses in the stator core are calculated by using (17) and (18) in the Steinmetz equation and integrating over the stator volume:

$$P_c = C_m h_s \int_0^{2\pi} \int_{r_{si}}^{r_{sa}} f^\alpha \hat{B}^\beta r \, dr \, d\varphi. \tag{22}$$

4.3 Other losses

Losses in the stator and the rotor also occur due to manufacturing tolerances and current harmonics. The latter result in magnetic field components that do not rotate synchronously with the rotor, therefore, inducing eddy currents. An analytical approach for calculating the resulting rotor losses has been presented in [18]. Models for obtaining the stator losses caused by harmonics have also been presented in the literature, e.g. in [6] and [31]. As these losses largely depend on the modulation scheme and the switching frequency of the applied inverter system, they are not considered in the subsequent optimization.

4.4 Thermal model

The overall losses are ultimately limited by thermal constraints. The temperature θ of the stator is estimated based on a thermal model that accounts for heat transfer between the motor and its surrounding by convection and radiation. The model used for the design evaluation in Section 5 considers free convection for a vertically-aligned cylindrical motor and can easily be adjusted for other operating conditions, such as forced convection. Details regarding the heat transfer coefficients for such an arrangement under various conditions can be found in [36].

5. Design optimization

The design equations and loss models presented in Sections 3 and 4 are used to obtain an optimized motor design by following the procedure outlined in Fig. 4. The rotor diameter d_r, rotor height h_r, and required mechanical air gap δ_{mech} are used as geometrical
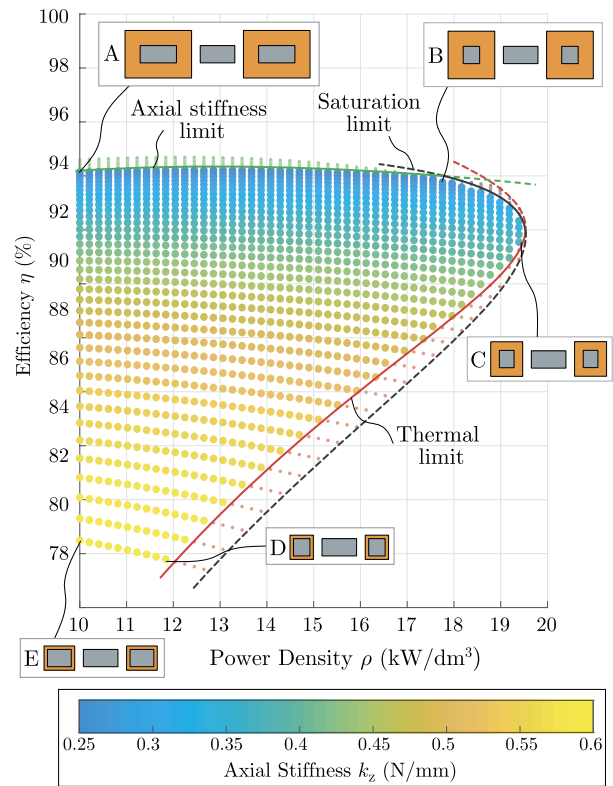
Fig. 5. Efficiency and power density of various motor designs including the Pareto front (Color figure online)

input parameters of the design flow. For a design with an a priori requirement for the rotational speed n_{max}, d_r can be obtained by (11). Design constraints are imposed by also providing the maximum admissible motor temperature θ_{max} as well as the material properties, including the saturation flux density B_{sat} of the stator. Constraints imposed by the maximum output current of the employed inverter system can be taken into account by providing the value for the current density in the coils according to $J = I_{max}/A_{cu}$. If the minimum required passive axial stiffness that the intended application imposes on the motor design is known, its value can also be input as a design constraint.

Initially, the height of the stator core is chosen as $h_s = h_r$. For this design, the coil width w_c and the width of the stator core w_s are varied within a meaningful range. Results can rapidly be obtained for a large number of designs based on the presented analytical models while taking the temperature dependency of the loss components into account. The calculation results yield a Pareto front in the performance space consisting of the power density ρ and the motor efficiency η.

In a subsequent step, the passive motor properties of selected designs can be assessed by means of 3D FEM simulations. An additional optimization of the passive axial stiffness k_z and tilting stiffness k_α can be carried out by adjusting the height of the stator core h_s. The iteration process of w_c and w_s can then be repeated for the new value of h_s as indicated by the dashed arrow in Fig. 4.

Figure 5 shows the results for an exemplary miniature high-speed motor that were obtained for the parameters listed in Table 3. Motor designs with power densities $\rho \in [10 \text{ kW/m}^3, 20 \text{ kW/m}^3]$ in steps of 0.2 kW/m^3 (50 linearly distributed data points) were evaluated. For each of the power densities, the coil width was varied as $w_c \in [0.125 \cdot r_r, 1.5 \cdot r_r]$, corresponding to $w_c \in [0.25 \text{ mm}, 3 \text{ mm}]$

Table 3. Design parameters used to obtain the results shown in Fig. 5

Parameter	Value	Parameter	Value
n_{max}	750 000 rpm	J	5 A/mm^2
d_r	4 mm	θ_{max}	65 °C
h_r	2 mm	B_{sat}	1.56 T [19]
δ_{mech}	1 mm		

for the chosen design parameters, in 50 logarithmically distributed steps. The value of w_s was adjusted accordingly for each data point as a dependent parameter. In total, 2500 different designs were evaluated. It can be observed that the achievable power density is limited by thermal constraints, which are more restrictive than the limitation imposed by saturation of the stator core. The performance is only limited by saturation in a narrow range for high efficiencies. The efficiency is limited by the achievable passive axial stiffness of the motor designs, which is shown by the color scale.

Based on the schematic cross-sectional geometries of the motor designs, which are shown in the insets of Fig. 5 and labeled A-E, at different locations in the performance space, the basic design relations can be observed. Design A features high volumes of the stator core and coils, resulting in low core losses and low copper losses and, consequently, in a high efficiency. However, the power density is low and the large value of w_c causes a large magnetic air gap that results in a low value of k_z. Moving from design A toward design B, the power density is significantly increased while the efficiency remains approximately constant. The increased power density is achieved by a lower volume of the stator core, while the coil volume is not altered significantly. This shows that the contribution of the core losses to the overall losses is low for designs that feature high efficiencies. However, reducing the core volume further results in saturation. While design B represents a significantly better trade-off compared to design A, it still features a low axial stiffness. By reducing w_c and keeping the core volume similar to that of design B, design C that attains a higher value of k_z is obtained. This is achieved by a decreased magnetic air gap. Due to increased copper losses, the efficiency of this design is lower than that of designs A and B and a further increase of the power density is not possible due to thermal constraints. The designs labeled D and E feature a higher axial stiffness, which is achieved by further reducing the copper volume, thereby decreasing δ_{mag}. This comes at the cost of a significantly decreased efficiency due to high copper losses.

The outlined dependencies show that for a fixed set of input parameters, only low motor efficiencies can be obtained if a high axial stiffness is required by the intended application. In such applications, the usage of a different motor topology might be beneficial.

6. Prototype implementation

A prototype that was designed based on the outlined optimization procedure is presented in this section.

6.1 Motor

The motor design was first introduced in [30], which can be referred to for details regarding the implementation. The prototype is shown in Fig. 6(a). The rotor is a commercially available diametrically-magnetized N45 grade NdFeB cylindrical magnet with a diameter of $d_r = 4$ mm [12]. The achievable rotational speed is mechanically limited to $n_{max} \approx 760\,000$ rpm. Most mechanical parts, including the stator wall, were manufactured using 3D printing technology, which yields a compact design with an outer motor diameter of less than 30 mm, as shown in Fig. 6(b).
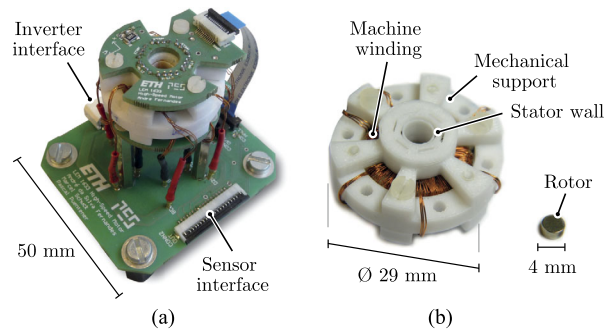
Fig. 6. Annotated photograph of the implemented motor prototype (a) and detailed view of the stator and the rotor (b)
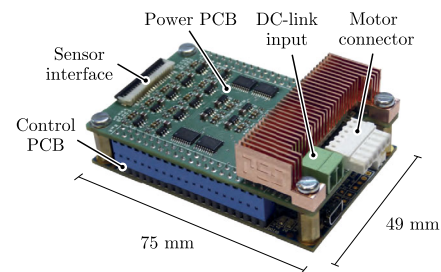
Fig. 7. Annotated photograph of the implemented inverter hardware

In [30], stable levitation was presented up to a rotational speed of 160 000 rpm at losses below 1 W. Even though the overall losses were at a low level, separation into their individual components by using the models provided in Section 4 shows that a large portion of the losses can be attributed to a significant harmonic content of the drive current. The achievable rotational speed was limited by the control bandwidth.

6.2 Inverter

These limitations imposed by high current harmonics and an insufficient control bandwidth require design considerations beyond those for the motor. The employed inverter is an essential part of the drive system and should feature a high power density to achieve a compact overall system. Design considerations for inverters of high-speed machines are presented in [31]. An exemplary inverter design intended for the use with the implemented motor prototype is shown in Fig. 7. It is based on six integrated half bridges of the type MPQ8039 [23] that drive the currents in the stator coils and allow for switching frequencies of several hundred kilohertz. By choosing the switching frequency sufficiently high compared to the synchronous rotational frequency (12.7 kHz at 760 000 rpm), the harmonic content and the associated losses can be reduced. The power electronics PCB is designed to fit on top of a control PCB. The latter comprises a field-programmable gate array (FPGA) that provides the required switching signals for pulse-width modulation along with fully digital implementations of the necessary motor controllers and sensor interfaces in hardware. Such an implementation allows for a high control bandwidth as required for achieving rotational speeds in the range of the mechanical limit of the rotor.

7. Conclusion

The slotless bearingless slice motor topology is well suited for miniaturization and achieving high rotational speeds. Direct scaling of the

motor geometry is limited by the requirements of the intended application and mechanical tolerances, resulting in a rapid increase of the relative magnetic air gap length for small motors. Design models, including those of the magnetic field in the machine, have been provided to assess the motor performance under these altered conditions. The optimization procedure presented in this work with a focus on miniature motors is universally applicable and clearly outlines the existing trade-offs between power density, motor efficiency, and passive stability properties, thereby facilitating the selection of Pareto-optimal designs. An exemplary implementation of a motor with a rotor diameter of 4 mm illustrates the downscaling potential of the considered bearingless slotless motor topology. Achieving rotational speeds in the range of several hundred thousand rpm requires a machine inverter that operates at a high switching frequency to limit harmonic losses in the motor. Furthermore, a high control bandwidth for the magnetic bearing is required. An example of a suitable inverter design has been shown and will be analyzed further with regard to the operation of the motor prototype.

Acknowledgements

References

1. Baumgartner, T., Kolar, J. W. (2015): Multivariable state feedback control of a 500 000-r/min self-bearing permanent-magnet motor. IEEE/ASME Trans. Mechatron., 20(3), 1149–1159. https://doi.org/10.1109/TMECH.2014.2323944.

2. Bertotti, G. (1988): General properties of power losses in soft ferromagnetic materials. IEEE Trans. Magn., 24(1), 621–630. https://doi.org/10.1109/20.43994.

3. Bilgen, E., Boulos, R. (1973): Functional dependence of torque coefficient of coaxial cylinders on gap width and Reynolds numbers. J. Fluids Eng., 95(1), 122–126.

4. Borisavljevic, A., Polinder, H., Ferreira, J. A. (2010): On the speed limits of permanent-magnet machines. IEEE Trans. Ind. Electron., 57(1), 220–227. https://doi.org/10.1109/TIE.2009.2030762.

5. Daily, J. W., Nece, R. E. (1960): Chamber dimension effects on induced flow and frictional resistance of enclosed rotating disks. J. Basic Eng., 82(1), 217–230. https://doi.org/10.1115/1.3662532.

6. Deng, F. (1997): Commutation-caused eddy-current losses in permanent-magnet brushless DC motors. IEEE Trans. Magn., 33(5), 4310–4318. https://doi.org/10.1109/20.620440.

7. Duma, V. F., Podoleanu, A. G. (2013): Polygon mirror scanners in biomedical imaging: a review. In Optical Components and Materials X (Vol. 8621). Bellingham: SPIE. https://doi.org/10.1117/12.2005065.

8. Epstein, A. H. (2004): Millimeter-scale, micro-electro-mechanical systems gas turbine engines. J. Eng. Gas Turbines Power, 126(2), 205–226. https://doi.org/10.1115/1.1739245.

9. Fausz, J., Wilson, B., Hall, C., Richie, D., Lappas, V. (2009): Survey of technology developments in flywheel attitude control and energy storage systems. J. Guid. Control Dyn., 32(2), 354–365. https://doi.org/10.2514/1.32092.

10. Ferreira, J. A. (1989): Electromagnetic Modelling of Power Electronic Converters. Berlin: Springer.

11. Hearn, E. J. (1997): Mechanics of Materials 2: The Mechanics of Elastic and Plastic Deformation of Solids and Structural Materials. 3rd ed. Stoneham: Butterworth.

12. HKCM Engineering (2016): Magnet-Disc S04x02ND-45SH Datasheet.

13. Kaufmann, M., Tüysüz, A., Kolar, J. W., Zwyssig, C. (2016): High-speed magnetically levitated reaction wheels for small satellites. In Proc. Int. Symp. Power Electronics, Electrical Drives Automation and Motion (SPEEDAM) 2016 (pp. 28–33). https://doi.org/10.1109/SPEEDAM.2016.7525889.

14. Kimman, M., Langen, H., Schmidt, R. M. (2010): A miniature milling spindle with active magnetic bearings. Mechatronics, 20(2), 224–235. https://doi.org/10.1016/j.mechatronics.2009.11.010.

15. Krahenbuhl, D., Zwyssig, C., Weser, H., Kolar, J. W. (2010): A miniature 500 000-r/min electrically driven turbocompressor. IEEE Trans. Ind. Appl., 46(6), 2459–2466. https://doi.org/10.1109/TIA.2010.2073673.

16. Looser, A., Tüysüz, A., Zwyssig, C., Kolar, J. W. (2017): Active magnetic damper for ultrahigh-speed permanent-magnet machines with gas bearings. IEEE Trans. Ind. Electron., 64(4), 2982–2991. https://doi.org/10.1109/tie.2016.2632680.

17. Luomi, J., Zwyssig, C., Looser, A., Kolar, J. W. (2009): Efficiency optimization of a 100-W 500 000-r/min permanent-magnet machine including air-friction losses. IEEE Trans. Ind. Appl., 45(4), 1368–1377. https://doi.org/10.1109/TIA.2009.2023492.

18. Markovic, M., Perriard, Y. (2008): Analytical solution for rotor eddy-current losses in a slotless permanent-magnet motor: The case of current sheet excitation. IEEE Trans. Magn., 44(3), 386–393. https://doi.org/10.1109/TMAG.2007.914620.

19. Metglas, Conway, SC, USA (2011): 2605SA1 Magnetic Alloy. https://metglas.com/wp-content/uploads/2016/12/Amorphous-Alloys-for-Transformer-Cores-.pdf

20. Mitterhofer, H., Gruber, W. (2017): Effizienzsteigerung durch die und in der Magnetlagertechnik. E&I, Elektrotech. Inf.tech., 134(2), 191–196. https://doi.org/10.1007/s00502-017-0487-1.

21. Mitterhofer, H., Gruber, W., Amrhein, W. (2014): On the high speed capacity of bearingless drives. IEEE Trans. Ind. Electron., 61(6), 3119–3126. https://doi.org/10.1109/TIE.2013.2272281.

22. Mitterhofer, H., Jungmayr, G., Amrhein, W., Davey, K. (2018): Coaxial tilt damping coil with additional active actuation capabilities. IEEE Trans. Ind. Appl., 54(6), 5879–5887. https://doi.org/10.1109/TIA.2018.2854263.

23. Monolithic Power Systems, Inc. (2016): MPQ8039 High Current Power Half Bridge.

24. Murgatroyd, P. N. (1989): Calculation of proximity losses in multistranded conductor bunches. IEE Proc. A, Phys. Sci. Meas. Instrum. Manag. Educ., 136(3), 115–120. https://doi.org/10.1049/ip-a-2.1989.0021.

25. Pfister, P. D., Perriard, Y. (2011): Slotless permanent-magnet machines: General analytical magnetic field calculation. IEEE Trans. Magn., 47(6), 1739–1752. https://doi.org/10.1109/TMAG.2011.2113396.

26. Puentener, P., Schuck, M., Steinert, D., Nussbaumer, T., Kolar, J. W. (2018): A 150000 rpm bearingless slice motor. IEEE/ASME Trans. Mechatron. https://doi.org/10.1109/TMECH.2018.2873894.

27. Raggl, K., Nussbaumer, T., Kolar, J. W. (2009): A comparison of separated and combined winding concepts for bearingless centrifugal pumps. J. Power Electron., 9(2), 243–258.

28. Rahman, M. A., Chiba, A., Fukao, T. (2004): Super high speed electrical machines—summary. In Proc. IEEE Power Engineering Society General Meeting (Vol. 2, pp. 1272–1275). https://doi.org/10.1109/PES.2004.1373062.

29. Schoeb, R., Barletta, N. (1997): Principle and application of a bearingless slice motor. JSME Int. J., Ser. C, Mech. Syst. Mach. Elem. Manuf., 40(4), 593–598.

30. Schuck, M., Da Silva Fernandes, A., Steinert, D., Kolar, J. W. (2017): A high speed millimeter-scale slotless bearingless slice motor. In Electric Machines and Drives Conference (IEMDC) 2017 (pp. 1–7). New York: IEEE Press.

31. Schwager, L., Tüysüz, A., Zwyssig, C., Kolar, J. W. (2014): Modeling and comparison of machine and converter losses for PWM and PAM in high-speed drives. IEEE Trans. Ind. Appl., 50(2), 995–1006. https://doi.org/10.1109/TIA.2013.2272711.

32. Schweitzer, G., Maslen, E. (2009): Magnetic bearings, theory, design, and application. Heidelberg: Springer.

33. Silber, S., Sloupensky, J., Dirnberger, P., Moravec, M., Amrhein, W., Reisinger, M. (2014): High-speed drive for textile rotor spinning applications. IEEE Trans. Ind. Electron., 61(6), 2990–2997. https://doi.org/10.1109/TIE.2013.2258308.

34. Steinert, D., Nussbaumer, T., Kolar, J. W. (2013): Concept of a 150 krpm bearingless slotless disc drive with combined windings. In Proc. Int. Electric Machines Drives Conf. (pp. 311–318). https://doi.org/10.1109/IEMDC.2013.6556269.

35. Steinert, D., Nussbaumer, T., Kolar, J. W. (2014): Slotless bearingless disk drive for high-speed and high-purity applications. IEEE Trans. Ind. Electron., 61(11), 5974–5986. https://doi.org/10.1109/TIE.2014.2311379.

36. VDI-Gesellschaft Verfahrenstechnik und Chemieingenieurswesen (2010): VDI Heat Atlas. 2nd ed. Berlin: Springer.

37. Zwyssig, C., Baumgartner, T., Kolar, J. W. (2014): High-speed magnetically levitated reaction wheel demonstrator. In Proc. Int. Power Electronics Conf. (IPEC-Hiroshima 2014—ECCE ASIA) (pp. 1707–1714). https://doi.org/10.1109/IPEC.2014.6869813.

38. Zwyssig, C., Kolar, J., Round, S. (2009): Megaspeed drive systems: Pushing beyond 1 million r/min. IEEE/ASME Trans. Mechatron., 14(5), 564–574. https://doi.org/10.1109/TMECH.2008.2009310.

Authors

Marcel Schuck

received the B. Sc. degree in electrical and computer engineering from the Technische Universität Darmstadt, Germany, in 2011 and the M. Sc. degree in the same field from the University of Illinois at Urbana-Champaign, USA, in 2013. He received an MBA degree from the Collège des Ingénieurs in Paris, France in 2014. He was a Ph.D. student at the Power Electronic Systems Laboratory at ETH Zurich, Switzerland from 2014 to 2017, where he is currently working as a postdoctoral researcher. His research interests include ultra-high speed bearingless machines, acoustic levitation, and mechatronic systems.

Pascal Puentener

was born in Erstfeld, Switzerland, in 1989. He studied mechanical and process engineering at the Swiss Federal Institute of Technology Zurich (ETH Zurich), Zurich, Switzerland, where he focused on dynamics and control theory. He carried out his master thesis in cooperation with an industry partner on robust control of a plant with uncertain resonance. After receiving his MSc degree in October 2015, he joined the Power Electronic Systems Laboratory as a PhD student.

Thomas Holenstein

was born in 1984 in St. Gallen, Switzerland, received the M. Sc degree in electrical engineering and information technology from the ETH Zurich, Switzerland, in 2009. During his studies, he focused on power electronics and mechatronics. In his master thesis, he developed new control algorithms for magnetically levitated motors. Since 2010 he has been working as an R&D engineer with the company Levitronix. Since 2015 he has been a Ph.D. student at the Power Electronic Systems Laboratory, ETH Zurich, where he is working on new motor concepts for magnetically levitated single-use drives.

Johann W. Kolar

received the M. Sc. and Ph. D. degrees (summa cum laude) from Vienna University of Technology, Vienna, Austria. He is currently a Full Professor with and the Head of the Power Electronic Systems Laboratory, Swiss Federal Institute of Technology Zurich (ETH Zurich), Zurich, Switzerland. He has proposed numerous novel pulsewidth-modulation converter topologies and modulation and control concepts, published more than 650 scientific papers in international journals and conference proceedings, and filed more than 110 patents. The focus of his current research is on ultracompact and ultraefficient converter topologies employing latest power semiconductor technology (SiC and GaN), wireless power transfer, solid-state transformers, power supplies on chip, and ultra-high speed and bearingless motors. Prof. Kolar was a recipient of 21 IEEE TRANSACTIONS and conference prize paper awards, the 2014 SEMIKRON Innovation Award, the 2014 IEEE Power Electronics Society R. David Middlebrook Award, and the ETH Zurich Golden Owl Award for Excellence in Teaching.